Characterization of the INFN proton CT scanner for cross-calibration of x-ray CT

Elena Fogazzi, Diego Trevisan, Paolo Farace, Roberto Righetto, Simon Rit, Monica Scaringella, Mara Bruzzi, Francesco Tommasino, Carlo Civinini

IOP Publishing Phys. Med. Biol. 68 (2023) 124001 https://doi.org/10.1088/1361-6560/acd6d3

Physics in Medicine & Biology

IPEM Institute of Physics and Engineering in Medicine

OPEN ACCESS

RECEIVED
23 February 2023

REVISED
4 May 2023

ACCEPTED FOR PUBLICATION
18 May 2023

PUBLISHED
7 June 2023

PAPER

Characterization of the INFN proton CT scanner for cross-calibration of x-ray CT

Elena Fogazzi[1,2], Diego Trevisan[3], Paolo Farace[2,3], Roberto Righetto[2,3], Simon Rit[4], Monica Scaringella[5], Mara Bruzzi[5,6], Francesco Tommasino[1,2,*] and Carlo Civinini[5]

[1] Physics department, University of Trento, via Sommarive 14, Povo (Tn), Italy
[2] Trento Institute for Fundamental Physics and Applications (TIFPA), Italian National Institute of Nuclear Physics (INFN), via Sommarive, 14, Povo (Tn), Italy
[3] Medical Physics Unit, Hospital of Trento, Azienda Provinciale per i Servizi Sanitari (APSS), Via Paolo Orsi 1, Trento, Italy
[4] University of Lyon, INSA-Lyon, Université Claude Bernard Lyon 1, UJM-Saint Etienne, CNRS, Inserm, CREATIS, UMR 5220, U1294 F-69373, Lyon, France
[5] Italian National Institute of Nuclear Physics (INFN), Florence section, Via G. Sansone 1, Sesto Fiorentino (Fi), Italy
[6] Physics and Astronomy department, University of Florence, via G. Sansone 1, Sesto Fiorentino (Fi), Italy
[*] Author to whom any correspondence should be addressed.

E-mail: francesco.tommasino@unitn.it

Keywords: ion imaging, computed tomography, proton therapy, image quality

Supplementary material for this article is available online

Abstract

Objective. The goal of this study was to assess the imaging performances of the pCT system developed in the framework of INFN-funded (Italian National Institute of Nuclear Physics) research projects. The spatial resolution, noise power spectrum (NPS) and RSP accuracy has been investigated, as a preliminary step to implement a new cross-calibration method for x-ray CT (xCT). *Approach*. The INFN pCT apparatus, made of four planes of silicon micro-strip detectors and a YAG:Ce scintillating calorimeter, reconstructs 3D RSP maps by a filtered-back projection algorithm. The imaging performances (i.e. spatial resolution, NPS and RSP accuracy) of the pCT system were assessed on a custom-made phantom, made of plastic materials with different densities ((0.66, 2.18) g cm^{-3}). For comparison, the same phantom was acquired with a clinical xCT system. *Main results*. The spatial resolution analysis revealed the nonlinearity of the imaging system, showing different imaging responses in air or water phantom background. Applying the Hann filter in the pCT reconstruction, it was possible to investigate the imaging potential of the system. Matching the spatial resolution value of the xCT (0.54 lp mm^{-1}) and acquiring both with the same dose level (11.6 mGy), the pCT appeared to be less noisy than xCT, with an RSP standard deviation of 0.0063. Concerning the RSP accuracy, the measured mean absolute percentage errors were (0.23+−0.09)% in air and (0.21+−0.07)% in water. *Significance*. The obtained performances confirm that the INFN pCT system provides a very accurate RSP estimation, appearing to be a feasible clinical tool for verification and correction of xCT calibration in proton treatment planning.

1. Introduction

Proton therapy (PT) is an established radiotherapy technique, thanks to its peculiar depth-dose profile (i.e. the Bragg peak) (Grau *et al* 2020). Although the high ballistic precision of PT represents its main advantage over photon treatments, it makes this technique more sensitive to uncertainties with respect to the planned target definition (Paganetti 2012). Hence, one of the current challenges in PT is the accurate description of body tissues, in terms of Relative (to water) stopping power (RSP), which finally determines the depth reached by protons inside the patient. The 3D RSP maps of the patients are currently calculated starting from the 3D Hounsfield unit (HU) map acquired with x-ray computed tomography (xCT), by means of semi-empirical methods. However, this conversion introduces non negligible uncertainties, which force to enlarge the

irradiated volume by adding safety margins, of the order of 3%–3.5% of the proton range, around target volumes (Schneider *et al* 1996, Yang *et al* 2010).

Proton CT (pCT) provides in principle the potential for a direct and more accurate estimation of the RSP and hence for improved treatment planning. However, many technical challenges remain to be solved, which so far hindered the clinical application of pCT. The maximum available proton beam energy (i.e. about 230 MeV, corresponding to about 32 cm in water) could limit the size of the object to be imaged and thus restrict pCT to volumes or treatment sites below this range threshold. Furthermore, the eventual integration of pCT systems in the clinics would further increase the cost of PT equipment, which is the main drawback compared to conventional photon therapy. Finally, but likely most critical, pCT is still in the development phase and it will take time before pCT scanners will be certified for the clinical use (Takada *et al* 1988, Johnson *et al* 2016, Pettersen *et al* 2017, Esposito *et al* 2018, Civinini *et al* 2020, DeJongh *et al* 2021b, Bär *et al* 2022, Granado-González *et al* 2022).

A recent study demonstrated that the ability to directly measure accurate RSP maps would enable pCT to be used for cross-calibration of the x-ray CT systems that are used for setting up the proton treatment plans (Farace *et al* 2021). This would be translated into a first clinical pCT application, without direct patient involvement. The purpose is to employ stabilised biological phantoms to mimic the proton beam interaction with human tissues. In fact, CT calibration is conventionally obtained by scanning a number of tissue equivalent materials, which have limitations in mimicking the radiobiological properties of real tissues and therefore introduce uncertainties in RSP estimation (Schaffner and Pedroni 1998). Trying to mitigate this issue, biological tissue samples were investigated for *ex vivo* validation (Möhler *et al* 2018, Xie *et al* 2018, Meijers *et al* 2020, Bär *et al* 2022). However, biological tissues are intrinsically heterogeneous, and uniform biological samples might be obtained only by homogenising tissue samples; this would mix all the different tissue components, modifying the tissue structure and properties, including the RSP. Considering such heterogeneity, it is expected that the most reliable RSP estimation would be directly obtained by pCT (DeJongh *et al* 2021a). The new calibration approach proposed in Farace *et al* (2021) relies on the possibility to acquire on the same biological phantom both the RSP and HU map, through the pCT system and the xCT system, respectively. By comparing the two tomographies voxel-by-voxel, a scatter plot is obtained (i.e. single-voxels RSP versus HU) and finally a cross-calibration curve can be extracted. Remarkably, once a reference pCT system is available, this procedure could be adopted by remote PT centres even when they are not equipped with a pCT system. This could be done by shipping a heterogeneous biological phantom to the remote centre, to be acquired with the xCT system to be calibrated, while having the corresponding RSP maps reconstructed from pCT measurements performed at the reference centre. The RPS map and the HU map are then processed and a calibration function specific for the remote xCT system can be extracted. The method was presented as a proof-of-principle in Farace *et al* (2021), deserving further improvements and refinements. In particular, the voxel-by-voxel comparison approach requires careful consideration of the differences between detectors and reconstruction algorithms of the two systems. Different levels of noise and spatial resolution are expected between the two tomographies. The different correlated blurring could introduce errors in the correlation between RSP and HU of each voxel. Therefore, understanding the imaging performances of the two systems is of paramount importance for a correct comparison of the two tomographies and for a correct estimation of the uncertainties in the extracted cross-calibration curve.

The present study aimed to assess the imaging performances of the INFN pCT system, in terms of spatial resolution, noise power spectrum (NPS) and RSP accuracy. This is a necessary preliminary analysis aiming at the implementation of the new procedure for cross-calibration of xCT. For this purpose, a custom-built synthetic phantom was proposed and imaged both with pCT and xCT systems at the Trento proton therapy centre (PTC).

2. Methods

2.1. pCT and xCT scanners and reconstructions

The INFN pCT system has been developed since 2006 in the framework of the PRIMA (PRoton IMAging) project funded by INFN (Civinini *et al* 2010, Scaringella *et al* 2013). The current system is a second generation apparatus and it is described in detail in Civinini *et al* (2020), with reconstruction methods updated in Scaringella *et al* (2023). The scanner is based on four planes of silicon micro-strip detectors, two upstream and two downstream with respect to the phantom to be imaged, which is placed on a remotely controlled rotating platform (figure 1). This configuration allows measuring the 3D coordinates and retrieving directions of the entry and exit points of each single proton in the phantom, required to reconstruct the most likely path (MLP) inside it (Schulte *et al* 2008). The residual energy of each proton is measured by a Cerium-doped Yttrium Aluminium Garnet (YAG:Ce) scintillating calorimeter, with a field of view (FOV) of 5×20 cm^2. A distance-driven filtered back-projection algorithm (Rit *et al* 2013), taking into account the single proton MLP and the residual energy, is applied to reconstruct the phantom 3D RSP map.

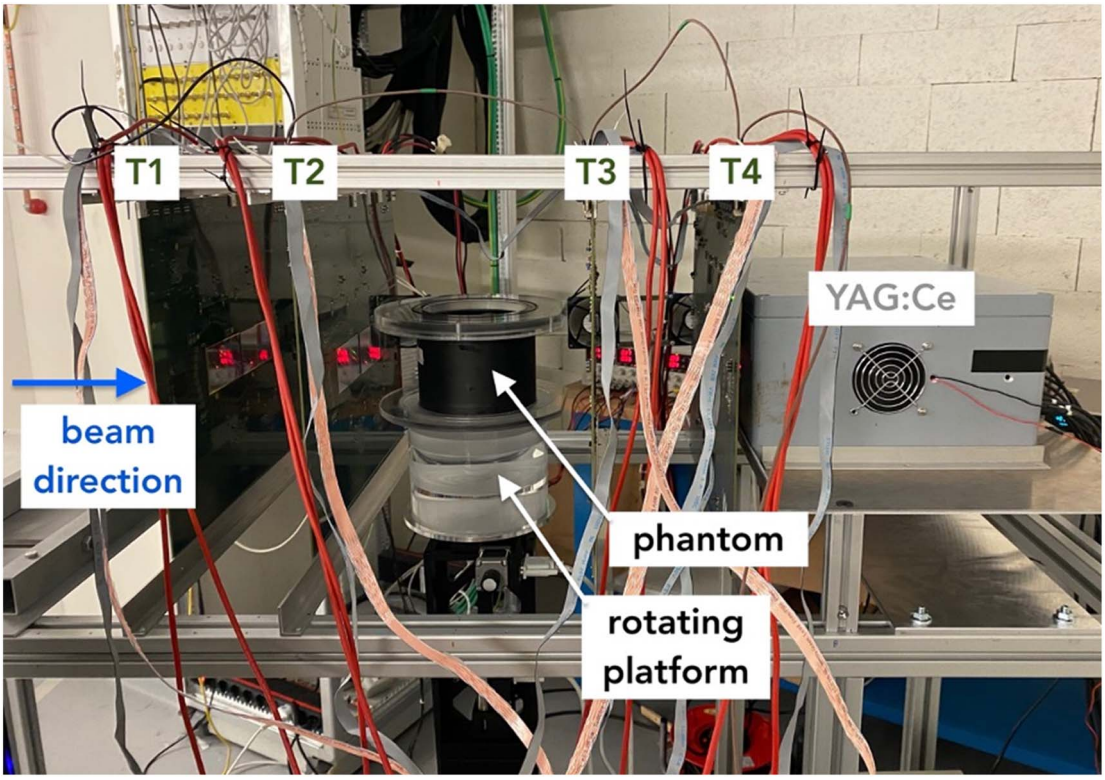

Figure 1. The INFN pCT scanner with its main parts labelled: four tracking planes (*T*), the YAG:Ce calorimeter and the phantom on the rotating platform. The exit beam pipe is placed 413 cm far from the first tracker plane and is not visible in the image, but the beam direction is indicated by the blue arrow. The distance between the first and the second tracker plane, as well as the one from the third and fourth, has been set to 15 cm. The space left free between the second and third plane, where the phantoms have been installed, was 30 cm.

The tomographies presented in this study were obtained with nine complete rotations of 0.9° angular steps, with acquisition rate of about 80–90 kHz. The total acquisition time for nine complete rotations is about 3 h. The total number of trigger events was 9×10^8, assumed to be a good statistics for high quality image output (Scaringella *et al* 2023). The scans have been performed at the experimental beam line at the Trento PTC (Tommasino *et al* 2017) at the nominal proton kinetic energy of 211.2 MeV. To cover the entire FOV of the pCT system, a 2.5 mm tantalum plate is placed at the exit of the beam pipe to enlarge the beam, as described in Civinini *et al* (2020). In the filtered back-projection algorithm, a Hann filter may be used instead of the conventional rectangular window at Nyquist's frequency (defined as $1/2s$ with s the pixel spacing of the projections). The cut-off frequency of the filter (f_{cut}), expressed as a fraction of Nyquist's frequency (f_{N}), can be adjusted in the range (0, 1). Since the reconstruction filter modulates the spatial frequency range both for signal and noise, we analysed image quality at different values of the filter parameter ($f_{\mathrm{cut}}/f_{\mathrm{N}}$), in order to find the best match of noise-spatial resolution tradeoff between pCT and xCT images and to build, at the same time, a look-up table useful for future applications.

The xCTs were acquired with a big bore Brilliance CT scanner (Philips Medical Systems, Cleveland, OH, USA) at the Trento PTC. To be closer to clinical scenarios, we decided to implement the standard acquisition protocol adopted for brain PT treatments. Namely, 120 kV x-ray beam with 0.563 scan pitch, 16×0.75 mm^2 collimation and 112 mAs exposure. This value of mAs was chosen in order to acquire the xCT images with a dose level comparable to that expected for the pCT statistics in this study: about 11.6 mGy, according to the dose estimation procedure described in Civinini *et al* (2017). To reconstruct the same FOV as the pCT system, the 512×512 acquisition matrix was reconstrued with a voxel size of $0.39 \times 0.39 \times 1.5$ mm^3, with the standard reconstruction kernel (UB). This voxel size is compatible with the ones normally used in the clinical protocol. A grid with the same dimensions was used for pCT reconstruction to facilitate the voxel-by-voxel comparison between proton and x-ray tomographies.

2.2. Image quality phantom

A specific phantom was designed and realised to investigate the pCT imaging performance in terms of spatial resolution, NPS and RSP accuracy (figure 2). The phantom has a cylindrical shape with 0.5 cm thick PMMA walls, 14 cm internal diameter and 13 cm height. Inside the phantom, five different cylindrical inserts of 3 cm

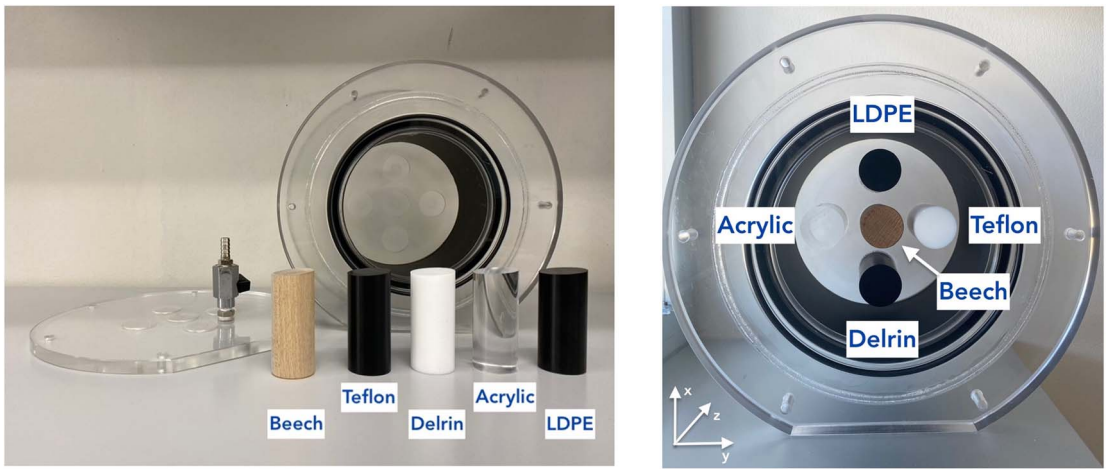

Figure 2. Custom-built image quality phantom. The upper cap of the phantom can be sealed thanks to a plastic gasket and six screws. The metallic vent valve on the cap allows additional air bubbles to escape after water filling and closure. Five cylinders can be inserted and fixed. The positions chosen for this study are shown in the *x*–*y* plane in the right picture.

diameter can be placed and fixed. Four synthetic plastic materials were chosen to resemble the density of different anatomical districts: Low-Density PolyEthylene (LDPE) (0.99 g cm^{-3}), Acrylic (1.20 g cm^{-3}), Delrin (1.41 g cm^{-3}), Teflon (2.18 g cm^{-3}). The fifth insert was made of beech wood that, as a low density (~0.66 g cm^{-3}) and inhomogeneous material, was exploited to preliminary and qualitatively probe the possible pCT system response to fatty and striated tissues which will be present in our future heterogeneous biological phantoms.

The phantom can be sealed on the top, in order to be employed with air or filled with (distilled) water. Hence, we could investigate the imaging performances at two different contrast-to-noise ratio levels. This allowed checking whether the response of the pCT system is linear, as is the case for the xCT system (Chen *et al* 2014)—that is, whether the spatial resolution of the system varies with the amount of noise and the contrast of the imaged object. Moreover, protons are expected to undergo different multiple-scattering in the two different background materials, resulting in different image quality.

Since all inserts were 6 cm high, the upper part of the cylinder was just air or water. In this way, homogeneous slices of water could be imaged to check the RSP value of water, that is the unity reference material, and the noise spectrum, as described in section 2.4.

2.3. Spatial resolution

The basic function that characterises the response of an imaging system is the modulation transfer function (MTF), which measures the spatial transfer characteristics of the system as a function of the spatial frequencies (Samei *et al* 2019).

Various methods have been proposed to measure the MTF, such as the use of slits, edges or bar pattern images (Samei *et al* 2019). In this study, the circular edges of phantom inserts were exploited to investigate the system response both symmetrically in the *x*–*y* plane and at different contrast and noise levels. This method was introduced by Richard *et al* (2012) and further refined by Chen *et al* (2014), and it was adapted in this study in the following way, both for pCT and xCT images.

(1) A squared region of interest (ROI), centred on the cylindrical insert and with a side twice the insert's diameter, was extracted in the *x*–*y* plane for each insert. The edge spread function (ESF) was thus constructed by recovering all the ROI pixel values as a function of their radial distance from the centre. Note that this approach assumes that the spatial resolution is homogeneous along the insert circumference and averages out the variations observed by Khellaf *et al* (2019) on simulated data with ideal trackers mainly.

(2) The ESF was then oversampled. This step allows the estimation of the so-called *presampled MTF*. Namely, the presampled MTF does not retain the typical MTF dependence on the signal pattern and on its relative location with respect to the detector grid. Hence, it is not affected by aliasing artefacts arising from the sampling step and it is a specific feature of the detector under study. In this way, the resolution values extracted from the presampled MTF should be independent of the voxel size, at least under the Nyquist theorem constraint (Buhr *et al* 2003). In the following analysis, the ESF was rebinned into one tenth of the

voxel size in the *x–y* plane. This value has been provided in literature as a gold standard to avoid too noisy ESF, preserving at the same time the spatial frequency response (Samei *et al* 1998).

(3) The oversampled ESF obtained so far can be strongly affected by the noise of the imaging system. To avoid the resulting fluctuations, one should average the ESF over multiple slices. However, since a finite quantity of slices are available with our scanner, we introduced a regularisation on the ESF by imposing the monotonicity of the function. Actually, the monotonicity constraint is rephrased as a quadratic optimisation problem, as described in (Maidment *et al* 2003) and adapted through the Matlab® (The MathWorks.Inc., Natick, MA, USA) algorithm for constrained nonlinear multivariable function.

(4) To further reduce the noise impact, the ESF was then averaged over three non-consecutive slices. The number of slices is limited by the pCT FOV size. In particular, three groups of three non-consecutive slices each were extracted and the ESFs were averaged within the same group (ESF_{mean}). As a first approximation, this procedure was adopted to estimate the variability of the MTF values obtained with the same procedure. Then, the following step was performed for each group.

(5) Differentiating the ESF_{mean}, the line spread function (LSF) of the imaging system was obtained. By definition, the Fourier transform of the LSF is the MTF. As typically adopted for xCT systems (Samei *et al* 2019), the spatial resolution value was extracted from the spatial frequency corresponding to 10% of the MTF maximum value.

2.4. Noise power spectrum

The NPS was also investigated. The NPS magnitude reflects the level of stochastics fluctuations at each spatial frequency, and the integration for all nonzero frequencies yields the noise variance (Boedeker *et al* 2007). The shape of the NPS reveals the noise distribution in terms of spatial frequencies and the correlation between pixel values.

The 2D NPS was estimated through the method described by Boedeker *et al* (2007) and typically applied for conventional xCT scanners (Samei *et al* 2019). In order to investigate the noise characteristics across the entire FOV, nine 2.73 cm squared regions of interest (ROIs) were extracted within homogeneous water slices of the phantom as described in Samei *et al* (2019). Accordingly, the reliable NPS frequency range started at about 0.08 mm^{-1} and the noise was assumed to be wide-sense stationary within each small ROI.

The same ROIs were extracted for six slices along the rotation axis and subtraction of subsequent slices is performed for background removal before effectively calculating the NPS. This step allowed us to exclude the large-scale variations within each ROI. In fact, such variations are generally not considered noise, since they are not-stochastic. The choice of the background removal method has influence on the low-frequency domain of the NPS and the image subtraction method has been found to be one of the most accurate for xCT analysis (Dolly *et al* 2016). Hence, it was applied also for pCTs, to compare its response with the xCT one.

Finally, for ROI #*i* in a given *z* slice, the 2D NPS is defined as

$$\mathrm{NPS}_i(u, v) = |\mathrm{FFT}\{I(x, y) - I_{\mathrm{mean},i}\}|^2,$$

where $I(x, y)$ is the value of the pixel at position (x, y) in the *i*th ROI, and $I_{\mathrm{mean},\,i}$ is the pixel mean value of the *i*th ROI, subtracted to remove DC components in the Fourier Transform. The 2D NPS of the nine ROIs were then averaged and translated into 1D radial NPS. To improve the accuracy, the 1D radial NPS was averaged over the six available water slices.

2.5. RSP accuracy

The RSP accuracy was estimated both in case of air- and water-filled phantom, in the following way. For each plastic insert of the phantom, a circular ROI with 2 cm diameter is extracted for each slice, centred in the insert to avoid boundary effects. The mean of the values in the ROI of the *i*th slice ($RSP_{mean,\,i}$) was calculated and then averaged within ten slices (RSP_{mean}), to mitigate stochastic fluctuations:

$$\mathrm{RSP}_{\mathrm{mean}} = \frac{1}{N}\sum_{N}^{i=1} \mathrm{RSP}_{\mathrm{mean},\,i},$$

with $N = 10$ in this study. The uncertainty associated with $RSP_{mean,\,i}$ was the standard deviation of pixel values in the ROI of the *i*th slice, normalised by the square root of the number of pixels in that ROI. The uncertainty of RSP_{mean} was then obtained by error propagation. Finally, for each insert, the RSP accuracy was calculated as

$$\mathrm{RSP}_{\mathrm{acc}}(\%) = \frac{\mathrm{RSP}_{\mathrm{mean}} - \mathrm{RSP}_{\mathrm{ref}}}{\mathrm{RSP}_{\mathrm{ref}}} \times 100,$$

where RSP_{ref} was the reference value of RSP measured with a multilayer ionisation chamber (MLIC, Giraffe, IBA) at Trento PTC, as described in Fellin *et al* (2017). The pencil beam was set at four different energies (150,

170, 190, 210 MeV) to verify the robustness of the procedure. The targets were circular rods of the same materials of phantom inserts. In particular, rods of three different thicknesses (0.5, 1, 2 cm) were measured for each material, in order to exclude possible scattering effects due to the rod thickness. The uncertainty associated with the final RSP_{ref} values was the standard deviation of RSP values measured at different energies and with different rod thicknesses. The reported uncertainties on $RSP_{acc}(\%)$ were obtained by propagation of RSP_{mean} and RSP_{ref} errors.

The RSP accuracy was also estimated for water. In this case, the circular ROI had a 4 cm diameter and $RSP_{mean,\ i}$ was averaged over six slices. The reference RSP value for water was the expected one for liquid water at room temperature (~21 °C) according to (NIST) .

In addition, the mean absolute percentage error (MAPE) of the pCT scanner was estimated as $\mathrm{MAPE} = \frac{\sum_{j=1}^{n} | \mathrm{RSP}_{acc,\ j}(\%) |}{n}$ with n the total number of inserts. Namely, $n = 5$ for pCT images of the phantom filled with water, while $n = 4$ in case of air-filled phantom, since no water RSP values are measured.

3. Results

The imaging performances (i.e. spatial resolution and NPS) were analysed both for xCT and pCT images of the phantom (figure 3). Moreover, the accuracy of the RSP values reconstructed with the pCT was estimated in comparison with the MLIC measurements. As a first qualitative result, it was noticeable that both in xCT and pCT images the wood grains of the beech insert were clearly visible, validating a good response of the pCT system also to heterogeneous materials. In addition, some small air bubbles were distinguishable both in xCT and pCT with water background (figures 3(d)–(f)), proving that our system is sensitive even to 2 mm size details.

The LDPE insert was not visible in pCT images with water background (figures 3(e), (f)), making it difficult to estimate the spatial resolution at the corresponding density. In fact, as reported in section 3.3, the RSP of LDPE was really close to 1, and thus the ESF was nearly flat.

3.1. Spatial resolution

The spatial resolution was estimated for all inserts but LDPE, both with air and water background, The spatial resolution and by varying the filter parameter (f_{cut}/f_N) in the range (0.45, 1). Values lower than 0.45 were not investigated, since common xCT scanners have spatial resolution values well above 0.4 lp mm^{-1}, that is the spatial resolution obtained with $f_{cut}/f_N = 0.45$. As reported in figure 4 and in the *supplementary* tables TS1, TS2, for all inserts, the pCT resolution was not the same in the two background cases, implying a nonlinear response of the imaging system, unlike xCT systems using a filtered back-projection technique. The impact of the Hann filter was the same in both pCT images, i.e. the smoothing effect of the filter was much more evident as the cutoff-frequency decreased and the spatial resolution decreased. In figure 4, it is clear that with filter parameter $f_{cut}/f_N = 0.60$, the spatial resolution of the pCT images with air background was compatible with the one of xCT for all the inserts, within the uncertainties. While in case of water background, the optimal cut-off parameter for the pCT-xCT comparison seemed to be $f_{cut}/f_N = 0.65$.

3.2. Noise power spectrum

The noise magnitude and distribution were analysed through the uniform water slices within the phantom. As expected, the Hann filter had an impact on the NPS of the pCT images. Decreasing the cut-off filter frequency increases the blurring of the images, as previously reported, and at the same time it reduces the noise magnitude. This is visible in figure 5(a) and, more quantitatively, in table 1, where the integrals of the NPS curves, i.e. the standard deviation, were listed for the filter parameter varying in the range (0.45, 1). For the comparison pCT-xCT, the HU values were linearly rescaled by a factor 1000 to ensure concordance of NPS units (i.e. RSP^2mm^2). The standard deviation of the xCT was compatible with the one obtained with the pCT images with filter parameter 0.85, while it is greater than the one of pCT with filter parameter 0.65 by about 21%. The second effect of the filter application was the variation of the curve shape and especially of the frequency position of the NPS peak. In table 1, the peak position is reported as obtained from Gaussian fit of the peak region of the NPS curves with a confidence interval of 95%. As observed in figure 5(a), the peaks shifted toward lower frequency as the frequency parameter decreased. This variation was also visibly reflected in the noise appearance in the images, as reported in figures 5(b)–(d). The remarkable difference between the xCT and the pCT without applying the Hann filter clearly emerges from figure 5(a). With filter parameter equal to 0.65, the pCT frequency peak deviated from xCT by about 9% toward higher frequencies.

3.3. RSP accuracy

The MAPE was calculated both for air and water background pCTs, by varying the filter parameter (f_{cut}/f_N) in the range (0.45, 1) (table 2). It is noteworthy that all the MAPE values, for all the filter parameters and

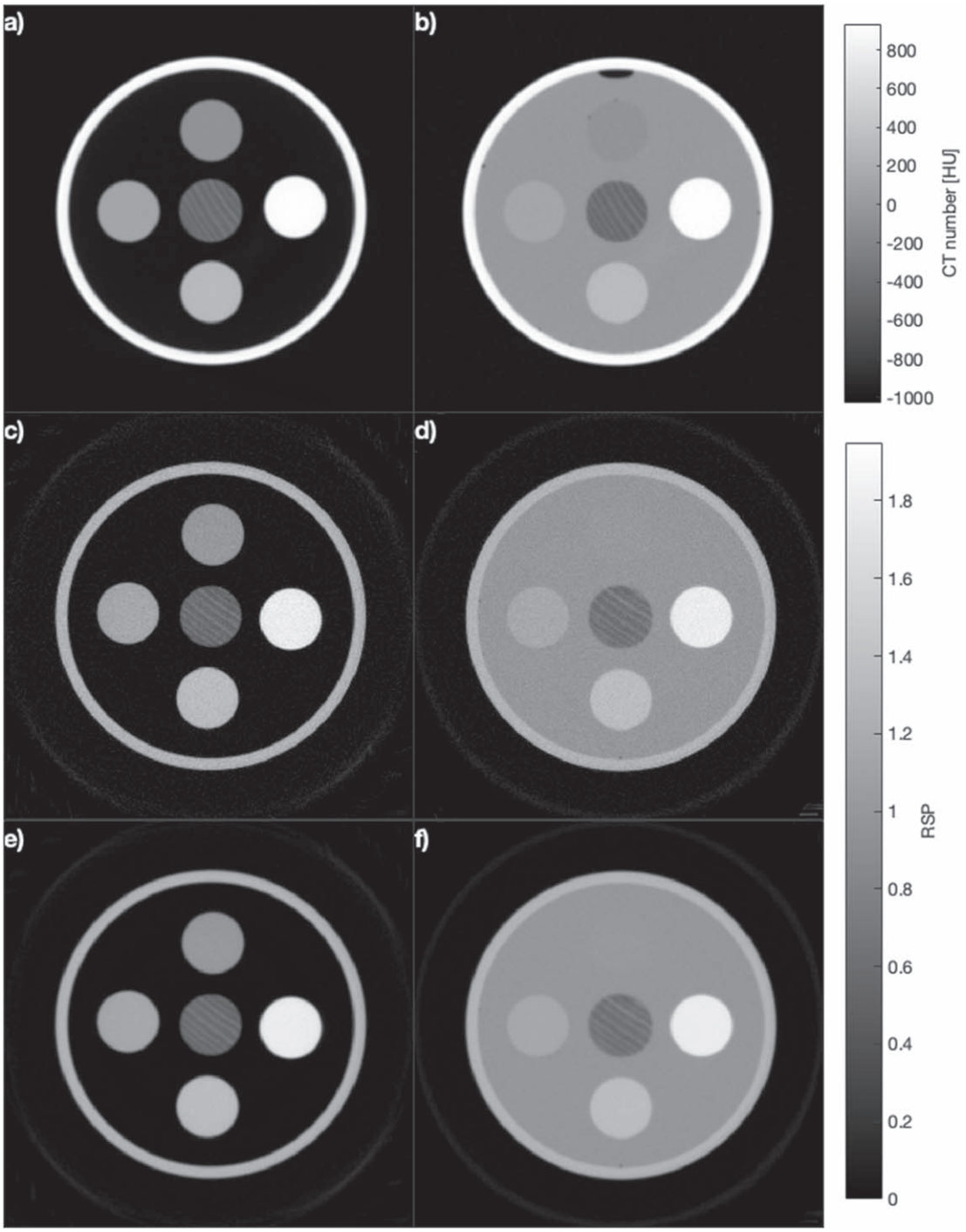

Figure 3. (a), (b) xCT, (c), (d) pCT without Hann windowing (e), (f) pCT with Hann windowing ($f_{cut}/f_N = 0.65$) of the image quality phantom, filled with air (a), (c), (e) or with water (b), (d), (f). The central slice along the cylinder length is displayed in all cases.

background cases, were compatible within uncertainties and are below 0.37%. For the filter $f_{cut}/f_N = 0.65$, the MAPEs are (0.23+−0.09)% in air and (0.21+−0.07)% in water. They were reported in figure 6, together with the RSP accuracy (%) values as function of the RSP values of the inserts.

4. Discussion

The INFN pCT system has been repeatedly tested at the Trento PT Centre (Civinini *et al* 2020, Farace *et al* 2021) and the calibration and reconstruction procedures have been recently updated and verified (Scaringella *et al* 2023). We are now designing a new implementation of the pCT system in proton treatment planning, based on the direct comparison between pCT and xCT to construct a cross-calibration curve. The procedure, already

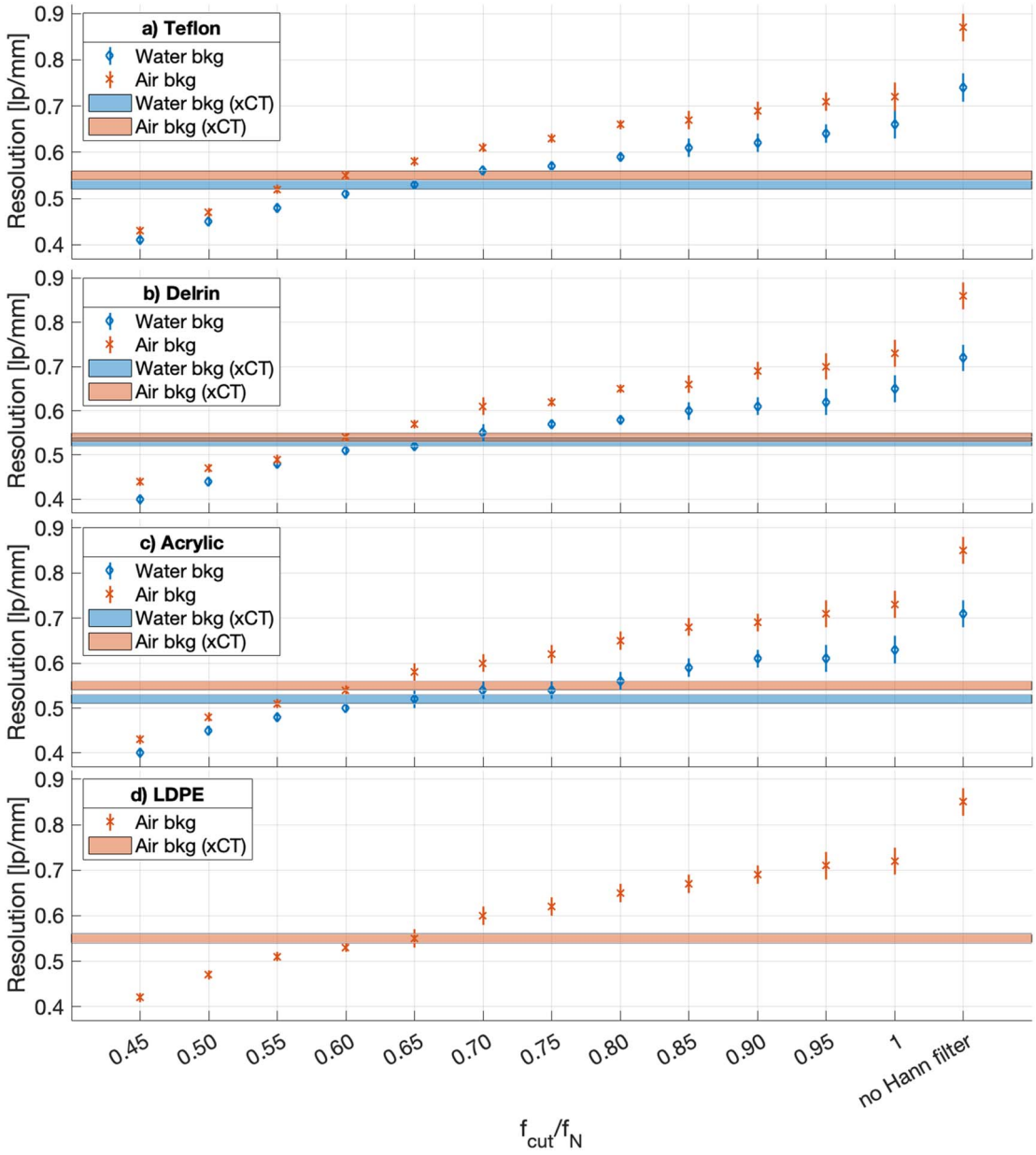

Figure 4. Spatial resolution values for Teflon, Delrin, Acrylic, LDPE for pCT images reconstructed with different filter parameters (f_{cut}/f_N), both in case of water and air background. The blue and red coloured bands represent the spatial resolution value of xCT images for each insert with water or air background, respectively.

proposed in Farace *et al* (2021), requires the pCT performance parameters to be extensively investigated as a preliminary step.

Therefore, in this study the imaging performance of the INFN pCT was investigated in terms of spatial resolution, NPS and RSP accuracy, through a custom-built, synthetic phantom. The phantom design is similar to the one already used in performance analysis of other particle CT systems (Johnson *et al* 2016, Volz *et al* 2021, Dedes *et al* 2022, Götz *et al* 2022). However, the possibility to fill the phantom with liquid water is a novelty, as a step toward more realistic clinical conditions and similarities to biological phantoms that will be used to further work on the cross-calibration curve. Moreover, by changing the background, we could investigate the linearity of the pCT response, relevant in the analysis of non-homogeneous, biological phantoms.

As first qualitative results, the phantom pCT images correctly reproduced the phantom geometry, with no visible artefacts. Differences of RSP values below 1% were not distinguishable by simple visual inspection, as demonstrated also by the difficult identification of the LDPE insert in the water-filled phantom (figure 3). However, small structures, such as air bubbles and wood grains, were clearly distinguishable, as they were in xCTs.

These aspects can be quantitatively assessed by means of the spatial resolution estimation. Exploiting the circular edges of the phantom inserts, the MTF was computed for each insert signal but the LDPE, both in air

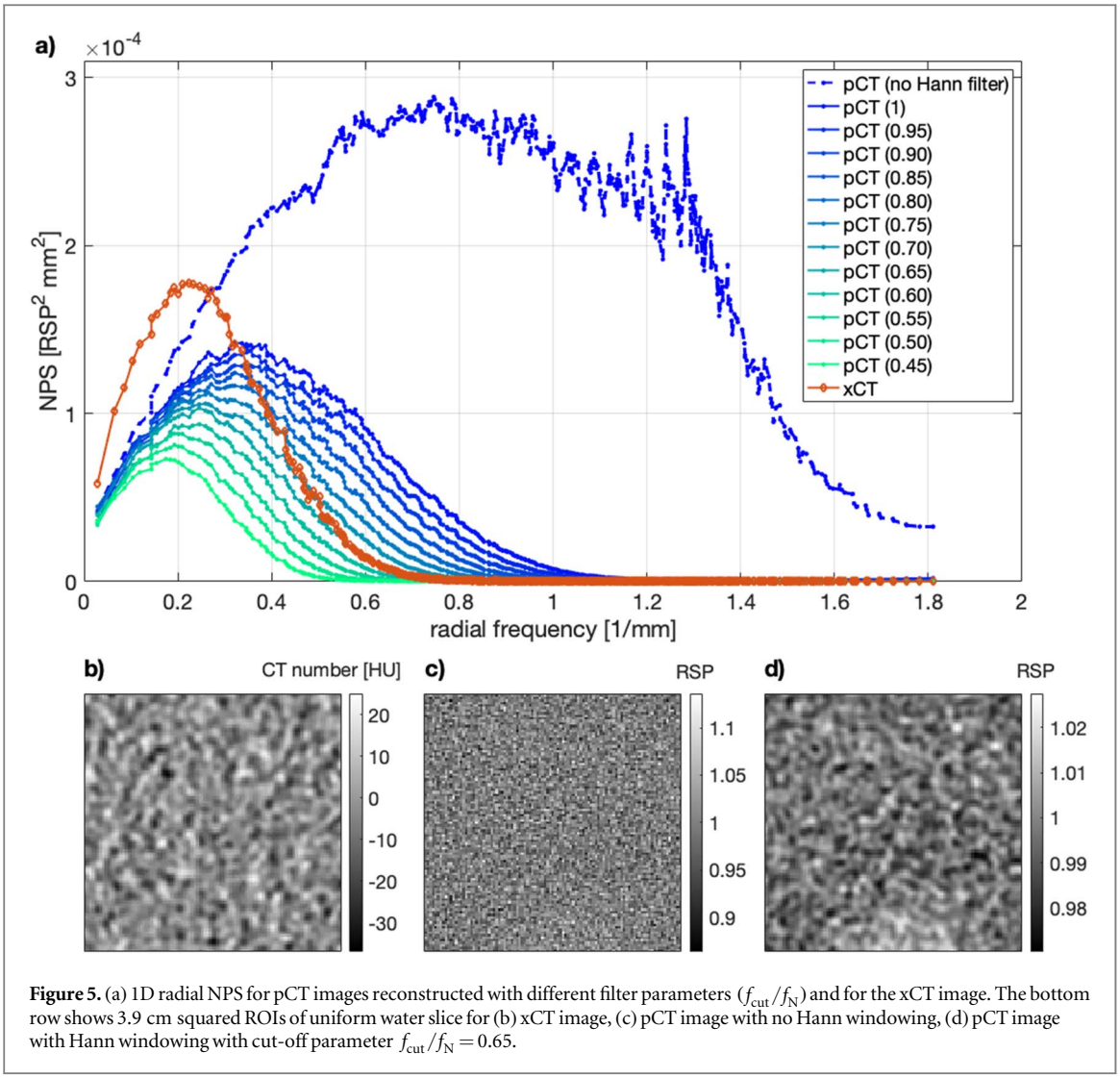

Figure 5. (a) 1D radial NPS for pCT images reconstructed with different filter parameters (f_{cut}/f_N) and for the xCT image. The bottom row shows 3.9 cm squared ROIs of uniform water slice for (b) xCT image, (c) pCT image with no Hann windowing, (d) pCT image with Hann windowing with cut-off parameter $f_{cut}/f_N = 0.65$.

Table 1. Standard deviation of pixel values estimated from the integral of the NPS curves and frequency position of the NPS peak estimated through Gaussian fit, for pCT images reconstructed with different filter parameters (f_{cut}/f_N) and the xCT image.

CT (f_{cut}/f_N)	Std (RSP)	Peak (mm^{-1})
pCT (no Hann filter)	0.0181	0.77 (0.01)
pCT (1)	0.0090	0.370 (0.003)
pCT (0.95)	0.0086	0.355 (0.003)
pCT (0.90)	0.0083	0.342 (0.003)
pCT (0.85)	0.0079	0.320 (0.003)
pCT (0.80)	0.0075	0.301 (0.003)
pCT (0.75)	0.0071	0.278 (0.003)
pCT (0.70)	0.0067	0.259 (0.003)
pCT (0.65)	0.0063	0.247 (0.002)
pCT (0.60)	0.0059	0.234 (0.002)
pCT (0.55)	0.0054	0.208 (0.002)
pCT (0.50)	0.0050	0.195 (0.002)
pCT (0.45)	0.0045	0.183 (0.002)
xCT	0.0080	0.224 (0.003)

and water background. The pCT images reconstructed with no Hann windowing had a clearly higher resolution than xCTs (figure 5). Moreover, both xCTs and pCTs were acquired at the same dose level (i.e. about 11.6 mGy), to compare their NPS. NPS is commonly assessed in xCT scanners characterization

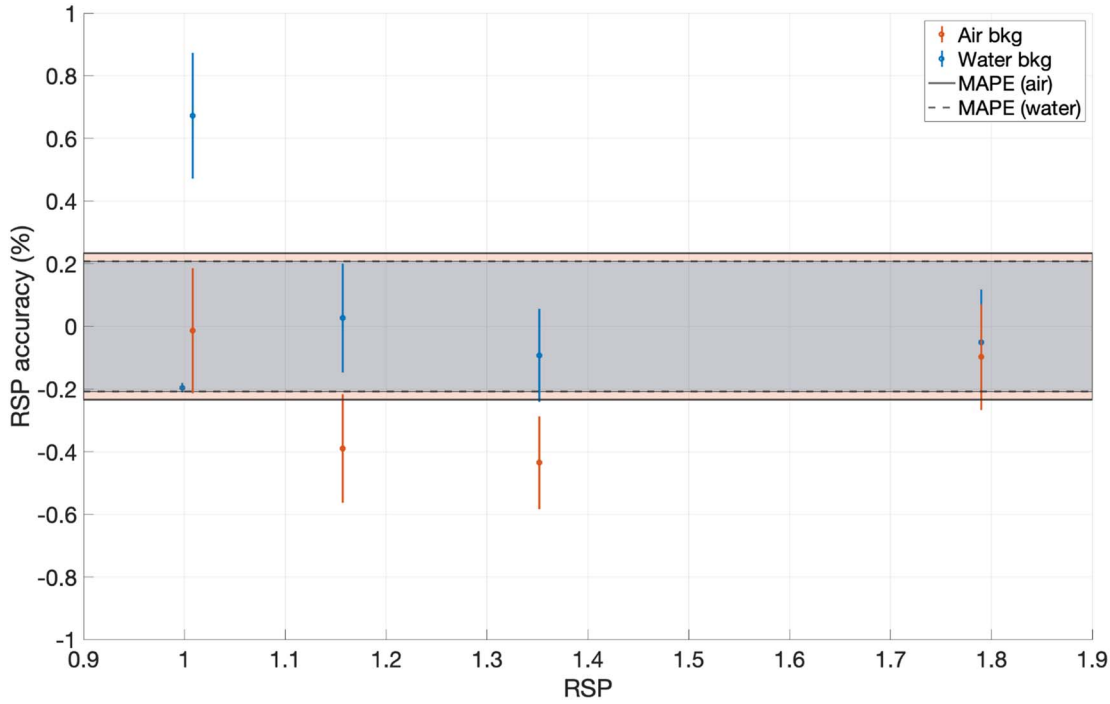

Figure 6. RSP accuracy (%) as a function of the RSP values of the cylindrical inserts and water, both in case of air and water background, for pCT images reconstructed with filter parameter $f_{cut}/f_N = 0.65$. The red and blue coloured bands signify the range (-MAPE, +MAPE) for air and water background, respectively.

Table 2. MAPEs of pCT images reconstructed with different filter parameters (f_{cut}/f_N).

CT (f_{cut}/f_N)	Air MAPE (%)	Water MAPE (%)
pCT (no Hann filter)	0.23 (0.09)	0.22 (0.07)
pCT (1)	0.23 (0.09)	0.21 (0.07)
pCT (0.95)	0.24 (0.09)	0.21 (0.07)
pCT (0.90)	0.24 (0.09)	0.23 (0.07)
pCT (0.85)	0.23 (0.09)	0.20 (0.07)
pCT (0.80)	0.23 (0.09)	0.23 (0.07)
pCT (0.75)	0.23 (0.09)	0.24 (0.07)
pCT (0.70)	0.26 (0.09)	0.21 (0.07)
pCT (0.65)	0.23 (0.09)	0.21 (0.07)
pCT (0.60)	0.23 (0.09)	0.23 (0.07)
pCT (0.55)	0.23 (0.09)	0.21 (0.07)
pCT (0.50)	0.22 (0.09)	0.20 (0.07)
pCT (0.45)	0.28 (0.09)	0.20 (0.07)

(Samei *et al* 2019), and, to our knowledge, this article reports it for the first time for a pCT scanner. The noise magnitude (i.e. standard deviation) of pCT images reconstructed without Hann windowing is significantly higher than xCTs (table 1). In addition, the pCT noise spectrum is shifted toward higher frequency. This is directly reflected in the image appearance, with a visible finer grain noise, revealing a higher correlation between nearest voxels (figure 5).

Furthermore, the pCTs were reconstructed with a Hann filter, varying the cut-off frequency to bring the imaging performance of the pCT system close to that of the xCT. As expected, the filter had a dual effect. On the one hand, it increased the blurring of the image, hence reducing the spatial resolution (figure 4). On the other hand, it considerably decreased the noise magnitude of the image, i.e. the standard deviation, shifting at the same time the peak of the noise spectrum to lower frequencies (figure 5, table 1).

Analysing the MTFs, it is noteworthy that the resolution level of the pCT system was different in the two background conditions (figure 4). This implies that the response of the system is nonlinear, in the sense that it depends on the level of noise and contrast, unlike the common xCT systems. The reason is the enormous impact of multiple scattering on proton trajectory compared to the x-ray one, and also its dependence on the traversed

material. In the case of insert-air contrast, the suitable Hann filter parameter value for matching pCT-xCT resolution is 0.60. On the other hand, the filter parameter value 0.65 is more suitable in the case of insert-water contrast. At the same time, the analysis of the NPS revealed that pCT has some potential for dose reduction in CT. In fact, adjusting the Hann filter so that the pCT had the same spatial resolution as the xCT ($f_{cut}/f_N = 0.65$), at the same dose level the pCT images showed a lower noise magnitude than xCT (figure 5(a)). As result, at the same dose level, there is no filter parameter matching both the xCT spatial resolution level and noise spectrum. Matching resolution levels and keeping the noise as low as possible would minimise errors in the voxel by voxel correlation of RSP and HU. As part of the work for the new calibration procedure based on the stabilised biological phantoms, we will investigate the impact of different resolution and noise levels between imaging modalities on the cross-calibration curve.

Varying the filter parameter value, we investigated the performance potential of the INFN pCT scanner. Recently, (Dedes *et al* 2022) compared two other prototype scanners using the same reconstruction algorithm without Hann windowing and the same spatial resolution metric but different beams and phantoms. Comparing the spatial resolution of their Dentin insert (RSP 1.495) in a blue wax body (RSP 0.980) with our Delrin insert (RSP 1.3652) in water (RSP 0.998), they obtained 0.62 lp mm^{-1} and 0.44 lp mm^{-1} for the pCT collaboration and ProtonVDA scanners, respectively, while we measured 0.72 lp mm^{-1} with the INFN scanner. However, the two phantoms had different materials and sizes (diameters of 18 cm blue wax in their study and 14 cm water + 1 cm PMMA in ours) and the insert distances from the phantom surfaces were different (about 3.2 and 3.5 cm), which are known to be two factors strongly influencing the spatial resolution in pCT (Krah *et al* 2018), together with many other factors such as beam quality and phantom positioning (Bopp *et al* 2014, Meyer *et al* 2020). Therefore, a direct comparison is not advisable. However, the obtained performance look-up tables allow us to easily adopt this analysis in future comparison between our pCT scanner and other xCT scanners for cross-calibration.

Above all, the accuracy of the RSP values reconstructed by pCT is of paramount importance in the characterization of our system, in order to accurately verify the calibration of the xCT scanner or their eventual cross-calibration. The previous analysis of pure water cylinders showed an accuracy well below 1% (Scaringella *et al* 2023). In this study, with much more complex geometry and different material densities, the RSP accuracy was well below 1% (see *supplementary material*, tables 3 and 4). The resulting MAPE values were compatible within the uncertainties for all the filter parameters, revealing that there is no dependency to the filter windowing within the range of tested values. Moreover, they were compatible for all the inserts in both background cases, proving that even with different phantom density (air or water), and therefore different residual energies, the calorimeter response reconstructs the same RSP values. This is a finer check of the calibration procedure than the one described in Scaringella *et al* (2023). In addition, the MAPE values, although achieved with a small number of materials, are lower than the one reported in Dedes *et al* (2022) and Götz *et al* (2022) with the same reconstruction algorithm, demonstrating a praiseworthy response of our detectors and calibration procedure.

Finally, the results obtained in this study, through the updated calibration and reconstruction procedures, placed our pCT system among the others currently working with above-average RSP accuracy values and no clearly visible artefacts. The acquisition rate of 80–90 kHz is lower than the one achieved by other systems (Dedes *et al* 2022) and, together with a limited FOV, it makes direct patient application of the INFN pCT impractical. However, we are working on introducing the INFN pCT scanner as a clinical tool for a novel verification and cross-calibration approach in the proton treatment planning (Farace *et al* 2021), acquiring both pCT and xCT tomographies on heterogeneous biological phantoms.

Generally speaking, further improvements to the pCT system performances could result from adopting an iterative reconstruction algorithm. In principle, this might translate into a reduction of noise in both xCT and pCT images. However, as recently shown by Hansen *et al* (2016), distance-driven algorithms are able to produce high quality pCT images, with a strong reduction of computational time (i.e. about a factor 22). At the same time, the use of ions heavier than protons (i.e. helium or carbon ions) would allow improving spatial resolution and potentially reduce imaging dose. While dose reduction is an aspect of potential interest for future applications, the absorbed dose is not critical for the current study, being focused on phantom investigation.

In conclusion, the extensive analysis performed in this study confirms that our pCT is extremely accurate and it can be used as a reference RSP measuring method for the verification of the xCT calibration in proton treatment planning by scanning a dedicated phantom. Further work on the cross-calibration curve is required to choose the appropriate comparison condition between pCT and xCT scans. Finally, despite the nonlinear resolution, our data demonstrated that pCT could have some potential for dose reduction in CT.

Acknowledgments

This work has been performed in the framework of the XpCalib experiment funded by INFN-CSN5. The authors would like to thank Dr Enrico Verroi for the fundamental technical support during the proton beam acquisitions.

Data availability statement

The data cannot be made publicly available upon publication because they are not available in a format that is sufficiently accessible or reusable by other researchers. The data that support the findings of this study are available upon reasonable request from the authors.

Declaration of interests

No conflict of interests to declare.

ORCID iDs

Elena Fogazzi https://orcid.org/0000-0002-2527-4070
Simon Rit https://orcid.org/0000-0003-2530-1013
Monica Scaringella https://orcid.org/0000-0002-6753-2832
Francesco Tommasino https://orcid.org/0000-0002-8684-9261
Carlo Civinini https://orcid.org/0000-0002-4952-3799

References

Bär E, Lennart V, Collins-Fekete C A, Brons S, Runz A and Schulte R W 2022 Experimental comparison of photon versus particle computed tomography to predict tissue relative stopping powers *Med. Phys.* **49** 474–87
Boedeker K L, Cooper V N and McNitt-Gray M F 2007 Application of the noise power spectrum in modern diagnostic MDCT: I. Measurement of noise power spectra and noise equivalent quanta *Phys. Med. Biol.* **52** 4027–46
Bopp C, Rescigno R, Rousseau M and Brasse D 2014 The impact of tracking system properties on the most likely path estimation in proton CT *Phys. Med. Biol.* **59** N197–210
Buhr E, Günther-Kohfahl S and Neitzel U 2003 Accuracy of a simple method for deriving the presampled modulation transfer function of a digital radiographic system from an edge image *Med. Phys.* **30** 2323–31
Chen B, Christianson O, Wilson J M and Samei E 2014 Assessment of volumetric noise and resolution performance for linear and nonlinear CT reconstruction methods *Med. Phys.* **41** 071909
Civinini C *et al* 2010 Towards a proton imaging system *Nucl. Instrum. Methods Phys. Res.* A **623** 588–90
Civinini C *et al* 2017 Proton computed tomography: iterative image reconstruction and dose evaluation *J. Instrum.* **12** C01034–01034
Civinini C *et al* 2020 Relative Stopping power measurements and prosthesis artifacts reduction in proton CT *Phys. Med. Biol.* **65** 225012
Dedes G *et al* 2022 Comparative accuracy and resolution assessment of two prototype proton computed tomography scanners *Med. Phys.* **49** 1–11
DeJongh D F *et al* 2021a A comparison of proton stopping power measured with proton CT and x-ray CT in fresh postmortem porcine structures *Med. Phys.* **48** 7998–8009
DeJongh E A *et al* 2021b Technical note: a fast and monolithic prototype clinical proton radiography system optimized for pencil beam scanning *Med. Phys.* **48** 1356–64
Dolly S, Chen H C, Anastasio M, Mutic S and HJJoacmp L 2016 Practical considerations for noise power spectra estimation for clinical CT scanners *J. Appl. Clin. Med. Phys.* **17** 392–407
Esposito M *et al* 2018 PRaVDA: the first solid state system for proton computed tomography *Phys. Med.* **55** 149–54
Farace P, Tommasino F, Righetto R, Fracchiolla F, Scaringella M, Bruzzi M and Civinini C 2021 Technical Note: CT calibration for proton treatment planning by cross-calibration with proton CT data *Med. Phys.* **48** 1349–55
Fellin F, Righetto R, Fava G, Trevisan D, Amelio D and Farace P 2017 Water equivalent thickness of immobilization devices in proton therapy planning - modelling at treatment planning and validation by measurements with a multi-layer ionization chamber *Phys. Med.* **35** 31–8
Götz S, Dickmann J, Rit S, Krah N, Khellaf F, Schulte R W, Parodi K, Dedes G and Landry G 2022 Evaluation of the impact of a scanner prototype on proton CT and helium CT image quality and dose efficiency with Monte Carlo simulation *Phys. Med. Biol.* **67** 055003
Granado-González M *et al* 2022 A novel range telescope concept for proton CT *Phys. Med. Biol.* **67** 035013
Grau C, Durante M, Georg D, Langendijk J A and Weber D C 2020 Particle therapy in Europe *Mol. Oncol.* **14** 1492–9
Hansen D C, Sørensen T S and Rit S 2016 Fast reconstruction of low dose proton CT by sinogram interpolation *Phys. Med. Biol.* **61** 5868
Johnson R P *et al* 2016 A fast experimental scanner for proton CT: technical performance and first experience with phantom scans *IEEE Trans. Nucl. Sci.* **63** 52–60
Khellaf F, Krah N, Rinaldi I, Létang J M and Rit S 2019 Effects of transverse heterogeneities on the most likely path of protons *Phys. Med. Biol.* **64** 065003
Krah N, Khellaf F, Létang J M, Rit S and Rinaldi I 2018 A comprehensive theoretical comparison of proton imaging set-ups in terms of spatial resolution *Phys. Med. Biol.* **63** 135013
Maidment A D and Albert M 2003 Conditioning data for calculation of the modulation transfer function *Med. Phys.* **30** 248–53

Meijers A, Free J, Wagenaar D, Deffet S, Knopf A C, Langendijk J A and Both S 2020 Validation of the proton range accuracy and optimization of CT calibration curves utilizing range probing *Phys. Med. Biol.* **65** 3

Meyer S, Bortfeldt J, Lämmer P, Englbrecht F S, Pinto M, Schnürle K, Würl M and Parodi K 2020 Optimization and performance study of a proton CT system for pre-clinical small animal imaging *Phys. Med. Biol.* **65** 155008

Möhler C, Russ T, Wohlfahrt P, Elter A, Runz A, Richter C and Greilich S 2018 Experimental verification of stopping-power prediction from single- and dual-energy computed tomography in biological tissues *Phys. Med. Biol.* **63** 025001

n.d. Retrieved from Pstar—Stopping-Power and Range Tables for Proton https://physics.nist.gov/PhysRefData/Star/Text/PSTAR.html 2023 NIST

Paganetti H 2012 Range uncertainties in proton therapy and the role of Monte Carlo simulations *Phys. Med. Biol.* **57** R99–117

Pettersen H *et al* 2017 Proton tracking in a high-granularity digital tracking calorimeter for proton CT purposed *Nucl. Instrum. Methods Phys. Res.* A **860** 51–61

Richard S, Husarik D B, Yadava G, Murphy S N and Samei E 2012 Towards task-based assessment of CT performance: system and object MTF across different reconstruction algorithms *Med. Phys.* **39** 4115–22

Rit S, Dedes G, Freud N, Sarrut D and Létang J M 2013 Filtered backprojection proton CT reconstruction along most likely paths *Med. Phys.* **40** 031103–1 – 031103

Samei E, Flynn M J and Reimann D A 1998 A method for measuring the presampled MTF of digital radiographic systems using an edge test device *Med. Phys.* **25** 102–13

Samei E *et al* 2019 Performance evaluation of computed tomography systems: summary of AAPM task group 233 *Med. Phys.* **46** E735–56

Scaringella M *et al* 2013 The PRIMA (PRoton IMAging) collaboration: development of a proton computed tomography apparatus *Nucl. Instrum. Methods Phys. Res.* A **730** 178–83

Scaringella M *et al* 2023 Relative stopping power measurement with the INFN proton computed tomography system: calibration and verification *Phys. Med. Biol.*

Schaffner B and Pedroni E 1998 The precision of proton range calculations in proton radiotherapy treatment planning: experimental verification of the relation between CT-HU and proton stopping power *Phys. Med. Biol.* **43** 1579

Schneider U, Pedroni E and Lomax A 1996 The calibration of CT Hounsfield units for radiotherapy treatment planning *Phys. Med. Biol.* **41** 111–24

Schulte R W, Penfold S N, Tafas J T and Schubert K E 2008 A maximum likelihood proton path formalism for application in proton *Med. Phys.* **35** 4849–56

Takada Y, Kondo K, Marume T, Nagayoshi K, Okada I and Takikawa K 1988 Proton computed tomography with a 250 MeV pulsed beam *Nucl. Instrum. Methods Phys. Res.* A **273** 410–22

Tommasino F *et al* 2017 Proton beam characterization in the experimental room of the Trento Proton Therapy facility *Nucl. Instrum. Methods Phys. Res.* A **869** 15–20

Volz L, Collins-Fekete C A, Bär E, Brons S, Graeff C, Johnson R P, Runz A, Sarosiek C, Schulte R W and Seco J 2021 The accuracy of helium ion CT based particle therapy range prediction: an experimental study comparing different particle and x-ray CT modalities *Phys. Med. Biol.* **66** 235010

Xie Y, Ainsley C, Yin L, Zou W, McDonough J, Solberg T D, Lin A and Teo B K 2018 *Ex vivo* validation of a stoichiometric dual energy CT proton stopping power ratio calibration *Phys. Med. Biol.* **63** 055016

Yang M, Virshup G, Clayton J, Zhu X R, Mohan R and Dong L 2010 Theoretical variance analysis of single- and dual-energy computed tomography methods for calculating proton stopping power ratios of biological tissues *Phys. Med. Biol.* **55** 1343–62